



Cite this: *Energy Environ. Sci.*, 2025, 18, 8575

## Interfacial phase regulation of flexible single-ion conducting block copolymer electrolytes ensuring ultra-stable lithium metal batteries

Yating Yu,<sup>†,a</sup> Sida Chen,<sup>†,a</sup> Hai-Peng Liang,<sup>b</sup> Ziqi Zhao,<sup>a</sup> Guangze Chu,<sup>a</sup> Ziting Zhi,<sup>a</sup> Xian-Ao Li,<sup>a</sup> Cheng Li,<sup>a</sup> Ruixin Li,<sup>a</sup> Xin Liu,<sup>a</sup> Minghua Chen,<sup>id,\*a</sup> Youzhi Xu,<sup>id,\*c</sup> Stefano Passerini<sup>id,\*def</sup> and Zhen Chen<sup>id,\*a</sup>

Single-ion conducting copolymer electrolytes (SIEPs) have significant potential for next-generation lithium metal batteries (LMBs). However, the unsatisfactory ionic conductivity, limited mechanical strength, and lack of insights into the lithium-ion transport mechanism hinder their wide applications in LMBs. In this regard, we develop a novel SIEP through tethering lithium 3-hydroxypropanesulfonyl-trifluoromethane-sulfonylimide onto a poly(vinylidene fluoride-co-trifluorochloroethylene)-based copolymer (PCL-SIEP). Molecular dynamics simulations reveal a unique transport pathway where fluorine atoms in the copolymer backbone interact with lithium-ions, serving as staging points for ion transport between adjacent sidechains. Compared with dual-ion conducting counterparts, PCL-SIEP exhibits significantly higher Young's modulus (28 vs. 17 GPa), tensile strength (20.65 vs. 5.65 MPa), and  $t_{Li^+}$  (0.94 vs. 0.39), achieving substantially prolonged lithium stripping-plating lifetime, ca. >3200 vs. 323 h. This is predominantly ascribed to the as-formed favorable solid electrolyte interphase with ideal constitutions—ultra-high LiF content in combination with Li<sub>2</sub>O, dynamically regulating uniform Li<sup>+</sup> flux and stabilizing the electrode|electrolyte interface. Thereby, PCL-SIEP demonstrates superior compatibility with both LiFePO<sub>4</sub> (LFP) and LiNi<sub>0.8</sub>Co<sub>0.1</sub>Mn<sub>0.1</sub>O<sub>2</sub> cathodes in full-cells, and achieves impressive performance even under high-loading conditions (15 mg cm<sup>-2</sup>), low-temperature (−30 °C), in trilayer bipolar stacking pouch full-cells, achieving an energy density of 245.88 Wh kg<sup>-1</sup>. These render PCL-SIEP a strong candidate for next-generation high-performance LMBs.

Received 8th May 2025,  
Accepted 1st August 2025

DOI: 10.1039/d5ee02503f

rsc.li/ees

### Broader context

The global transition toward electrified transportation, smart energy infrastructure, and high-efficiency renewable energy storage systems is driving an urgent need for next-generation lithium metal batteries (LMBs) with higher energy density and intrinsic safety. However, the practical deployment of LMBs remains hindered by the formation of lithium dendrites, which compromise safety by piercing separators and inducing short circuits, and by the use of flammable liquid electrolytes. Single-ion polymer electrolytes (SIEPs) offer a promising pathway to address both challenges by suppressing anion-induced concentration polarization and mitigating dendrite growth through high lithium-ion transference numbers. Yet, existing SIEPs often suffer from a trade-off between room-temperature ionic conductivity and mechanical robustness. In this work, we present a molecular design strategy that covalently integrates lithium salt anions into the polymer backbone, achieving a synergistic enhancement of ionic conductivity and mechanical strength while ensuring electrochemical stability and favorable interfacial compatibility. This approach provides a new paradigm for the design of high-performance SIEPs and represents a significant step toward the realization of safe, high-energy-density LMBs.

<sup>a</sup> Key Laboratory of Engineering Dielectric and Applications (Ministry of Education), School of Electrical and Electronic Engineering, Harbin University of Science and Technology, Harbin 150080, China. E-mail: chen.zhen@hrbust.edu.cn

<sup>b</sup> GBA Institute of Collaborative Innovation, Department of Materials and Chemical Engineering, Sino-Singapore Guangzhou Knowledge City (China), 510555, China

<sup>c</sup> College of Chemistry and Molecular Sciences, Henan University, Kaifeng 475004, China

<sup>d</sup> Helmholtz Institute Ulm (HIU), Ulm 89081, Germany

<sup>e</sup> Karlsruhe Institute of Technology (KIT), Karlsruhe 76021, Germany

<sup>f</sup> Austrian Institute of Technology (AIT), Center for Transportation Technologies, Giefinggasse 4, 1210 Wien, Austria

<sup>†</sup> Yating Yu and Sida Chen contributed equally to this work.

### Introduction

The global transition toward carbon neutrality is accelerating the demand for sustainable energy storage systems, particularly in renewable energy grids, electric vehicles (EVs),<sup>1</sup> and emerging sectors like low altitude mobility, which includes drones and air taxis. Lithium metal, featuring high specific capacity (3860 mAh g<sup>-1</sup>)<sup>2</sup> and the lowest electrochemical potential (−3.04 V vs. standard hydrogen electrode),<sup>3</sup> is a highly promising

anode material for next-generation lithium metal batteries (LMBs). Its potential to boost energy density makes it an ideal candidate for applications in EVs and advanced air mobility solutions, where high performance, safety, and weight reduction are critical.<sup>4</sup> However, conventional liquid electrolytes pose substantial safety concerns due to their volatility and flammability, underscoring the need for safer, more efficient solid-state electrolytes.<sup>5–7</sup>

Polymer electrolytes, known for their improved thermal stability and mechanical properties, have garnered significant attention.<sup>8,9</sup> Early polymer electrolytes, pioneered by Wright in 1973 using poly(ethylene oxide) matrices, demonstrated the potential of these materials.<sup>10</sup> However, conventional dual-ion polymer electrolytes (DIPEs), where both lithium-ions and anions move freely, face limitations due to low lithium-ion transference numbers ( $t_{\text{Li}^+} < 0.5$ ).<sup>11</sup> In DIPEs, the migration of anions is faster than that of lithium-ions, which leads to concentration gradients and dendrite growth, impeding battery performance and safety.<sup>12,13</sup> To address these issues, single-ion conducting polymer electrolytes (SIPEs) have emerged as a promising solution. By covalently tethering anions to the polymer backbone, SIPEs achieve nearly unity lithium-ion transference ( $t_{\text{Li}^+} \approx 1$ ), suppressing dendrite growth and improving lithium-ion transport, offering a pathway toward safer and higher-performance LMBs.<sup>14</sup>

SIPEs are known for their insufficient ionic conductivity and/or limited electrochemical stability against oxidation.<sup>15,16</sup> To overcome the limitation of low ionic conductivity, plasticizers such as organic solvents or ionic liquids are generally introduced.<sup>17–19</sup> Although these additives enhance ion mobility, they frequently compromise mechanical strength, leading to challenges in maintaining structural integrity during battery cycling.<sup>20,21</sup> G. Brunklaus *et al.*<sup>22</sup> synthesized a homopolymer single-ion conductor containing a polysulfonamide segment, achieving an ionic conductivity of  $0.52 \text{ mS cm}^{-1}$  after blending with poly(vinylidene fluoride-*co*-hexafluoropropylene) (PVDF-HFP) and incorporating a mixed solvent of ethylene carbonate and propylene carbonate (PC). While PVDF-HFP improves the film-forming ability and flexibility of the electrolyte, the trade-off between conductivity and mechanical stability remains. To overcome this issue, multi-block copolymers with tunable block sizes and constituents have been explored to balance ionic transport and mechanical strength.<sup>23</sup> For example, based on a three-step method, Zhou *et al.*<sup>24</sup> synthesized an SIPE by *in situ* copolymerization of lithium 1-[3-(methacryloyloxy)-propylsulfonyl]-1-(trifluoromethanesulfonyl)imide and pentaerythritol tetraacrylate monomers, achieving an ionic conductivity of  $2.24 \times 10^{-3} \text{ S cm}^{-1}$ , a fracture stress of  $4.7 \text{ MPa}$ , and a maximum strain of  $7.1\%$ . Similarly, Nguyen<sup>25</sup> and Chen *et al.*<sup>26</sup> designed a self-standing, nanostructured SIPE based on a multi-block *co*-poly(arylene ether sulfone) polymer backbone, covalently attached with lithium perfluorosulfonimide side chains. After plasticization, the electrolyte achieved an ionic conductivity of  $0.6 \text{ mS cm}^{-1}$  at  $20^\circ\text{C}$  and an electrochemical stability window of  $4.96 \text{ V}$ . However, despite their favorable properties, these materials usually involve complex synthesis procedures that pose challenges for large-scale production. Therefore, developing SIPEs that combine high ionic conductivity, high mechanical strength and ease

of preparation remains a major challenge. Additionally, the lithium-ion transport mechanism, a critical factor for optimizing electrolyte performance, is still underexplored.

In this study, we designed a cost-effective SIPE based on poly(vinylidene fluoride-*co*-trifluorochloroethylene) copolymer, integrating  $-\text{SO}_2\text{N}^-\text{SO}_2-$ , O-C-C-C, and C-F functional groups in the side chains through a straightforward synthetic process. The  $-\text{SO}_2\text{N}^-\text{SO}_2-$  anion exhibits highly delocalized negative charges, promoting efficient lithium-ion dissociation. The O-C-C-C flexible group promotes segmental movement of side chains. The  $-\text{CF}_3$  end groups significantly improve thermal and electrochemical stability,<sup>27</sup> while facilitating the formation of LiF-enriched solid electrolyte interphase (SEI). Compared with the controlled sample (denoted as PC/L-DIPE), which was prepared by simply mixing Li-salt with poly(vinylidene fluoride-*co*-trifluorochloroethylene) (PVDF-CTFE), this kind of design delivers superior mechanical strength, a near-unity  $t_{\text{Li}^+}$ , and a significant reduction in dendritic lithium growth. Furthermore, molecular dynamics simulations further decipher that fluorine atoms in the copolymer backbone act as staging points for lithium-ion transport between side chains, offering valuable insights into lithium-ion transport mechanisms. These properties lead to enhanced electrochemical performance in  $\text{Li}||\text{Li}$  symmetric cell,  $\text{Li}||\text{LiFePO}_4$  and  $\text{Li}||\text{LiNi}_{0.8}\text{Co}_{0.1}\text{Mn}_{0.1}\text{O}_2$  full-cell configurations, showcasing PCL-SIPE as a strong candidate for next-generation LMBs.

## Results

### Synthetic routes and characterizations of dry-PCL-SIPE and dry-PC/L-DIPE

Scheme S1A and B illustrate the synthetic routes of lithium salt, namely, lithium 3-hydroxypropanesulfonyl-trifluoromethane-sulfonylimide (LiHPSI), which was subsequently tethered onto the PVDF-CTFE copolymer backbone (Fig. 1A and Scheme S1C) *via* a Williamson reaction. To reasonably quantify the actual LiHPSI content in the polymer matrix, CHNS elemental analysis (EA) was performed on the dry-PC/L-DIPE and dry-PCL-SIPE samples, as summarized in Table S1. The results indicate that the actual LiHPSI content in dry-PC/L-DIPE is likely higher than that in dry-PCL-SIPE, primarily due to differences in reaction kinetics and solvation behaviour. Nuclear magnetic resonance (NMR) was performed to study the structures of 3-chloropropanesulfonyl chloride, 3-chloropropanesulfonyl-trifluoromethane-sulfonylimide (LiCPSI) and LiHPSI (Fig. 1B and Fig. S1). According to the  $^1\text{H}$  NMR spectra of LiCPSI and LiHPSI, the apparent chemical shift variations when compared to the peaks of the  $-\text{CH}_2-$  (1.94–2.04 ppm),  $-\text{CH}_2\text{S}$  (2.64–2.69 ppm), and  $-\text{CH}_2\text{Cl}$  (3.65–3.69 ppm) groups of 3-chloropropanesulfonyl chloride, indicate changes in the proton environments. In particular, compared to the Cl group in LiCPSI, the hydroxyl group in LiHPSI exhibits a weaker deshielding effect due to its smaller electronegativity, resulting in a lower chemical shift of the corresponding proton signals. Additionally, the  $^7\text{Li}$  NMR spectrum (Fig. S2) shows a peak at  $-0.93 \text{ ppm}$ , confirming the presence of



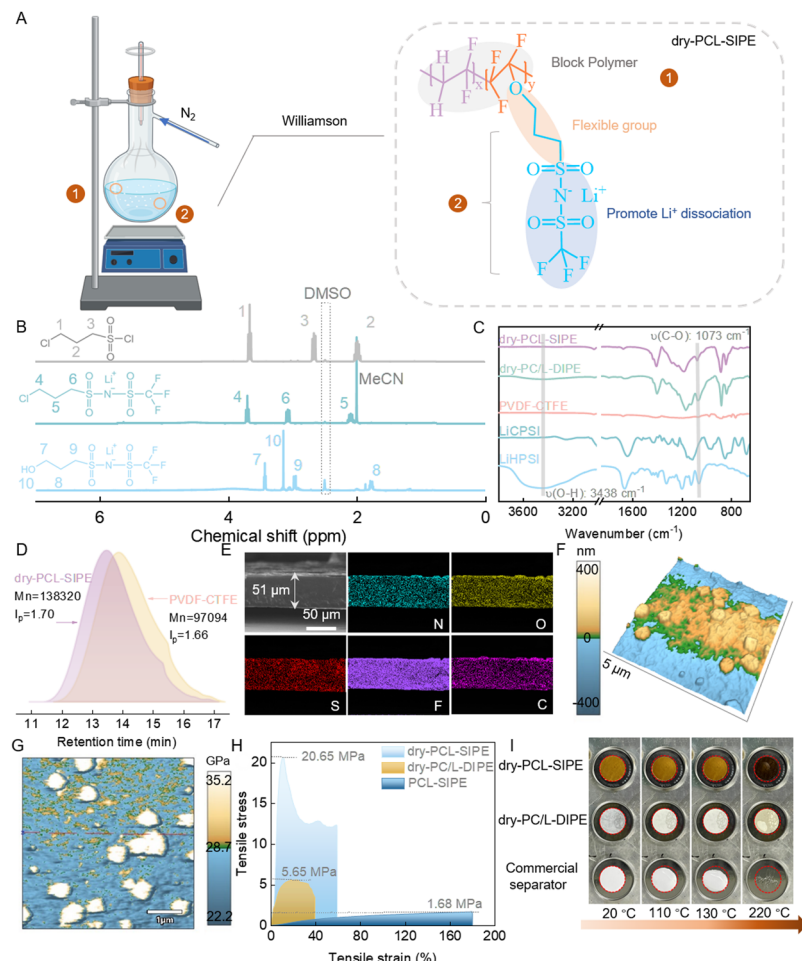


**Fig. 1** Synthesis and characterization of polymer electrolytes. (A) Synthetic illustration of dry-PCL-SIPE via the Williamson reaction. (B)  $^1\text{H}$  NMR spectra of 3-chloropropanesulfonyl chloride, LiCPSI and LiHPSI. (C) FT-IR spectra of LiCPSI, LiHPSI, PVDF-CTFE, dry-PCL-SIPE and dry-PC/L-DIPE (dry-PCL-SIPE and dry-PC/L-DIPE, both without PC). (D) GPC results of PVDF-CTFE and dry-PCL-SIPE. (E) SEM micrograph and its corresponding EDS mapping results of the dry-PCL-SIPE. (F) Investigation of surface morphology and (G) determination of Young's modulus for dry-PCL-SIPE via an AFM technique (the red line is the baseline of the Young's modulus). (H) Tensile strain–stress curves of the dry-PCL-SIPE, PCL-SIPE (with 61.5 wt% PC) and dry-PC/L-DIPE. (I) Digital photographs of dry-PCL-SIPE, dry-PC/L-DIPE, and a commercial separator after heating to different temperatures.

Li-ions in LiCPSI. In all three  $^1\text{H}$  NMR spectra, the area integration ratios of the peaks are 2:2:2, consistent with the expected chemical structure of the target products. According to the Fourier transform infrared spectra (FT-IR, Fig. 1C), the appearance of a broad  $-\text{OH}$  stretching vibration at  $3438\text{ cm}^{-1}$  and a distinct C–O stretching peak at  $1073\text{ cm}^{-1}$  in LiHPSI confirms the successful synthesis of LiHPSI from LiCPSI. Additionally, the disappearance of the  $-\text{OH}$  peak after the chemical grafting reaction onto the PVDF-CTFE backbone further validates the successful functionalization. Gel-permeation chromatography (GPC) results (Fig. 1D and Table S2) show that the dry-PCL-SIPE (refers to SIPE without PC) exhibits an increased average molecular number ( $M_n$ ) and average molecular weight ( $M_w$ ), and narrower molecular weight distribution, while maintaining the polydispersity index ( $I_p$ ) at 1.70.

The flatness and mechanical strength of SIPEs are critical in preventing the nucleation and growth of Li dendrites.<sup>28,29</sup> Compared to the dry-PC/L-DIPE (Fig. S3), the dry-PCL-SIPE exhibits significantly smoother and denser surface morphology.

This is further confirmed by cross-sectional scanning electron microscope (SEM) images and energy dispersive X-ray spectroscopy (EDS) analyses of dry-PCL-SIPE and dry-PC/L-DIPE (Fig. 1E and Fig. S4). The thickness of dry-PC/L-DIPE and dry-PCL-SIPE was estimated in the range of  $50 \pm 5\text{ }\mu\text{m}$ . The volume swelling behavior of the dry-PCL-SIPE membrane is displayed in Fig. S5. In addition, the compatibility between PC and dry-PCL-SIPE (or dry-PC/L-DIPE) is compared in Fig. S6. In the next step, the surface roughness of copolymer membranes was examined using atomic force microscopy (AFM). Evident from the representative images ( $5\text{ }\mu\text{m} \times 5\text{ }\mu\text{m}$ ) of the surface topography of the dry-PCL-SIPE and dry-PC/L-DIPE (Fig. 1F and Fig. S7A), their surface roughness was determined to be approximately 51.74 and 155.26 nm, respectively, in good agreement with the SEM observations. The smoother and denser structure of dry-PCL-SIPE enables better electrolyte/electrode contact and reduced interface impedance, both of which contribute positively to the battery performance. Furthermore, the dry-PCL-SIPE offers higher Young's modulus and tensile strength than the dry-PC/L-DIPE, *ca.*,

28 vs. 17 GPa and 20.65 vs. 5.65 MPa (Fig. 1G, H and Fig. S7B and S8), respectively. The tensile strength of dry-PCL-SIPE ranks among the top reported for SIPEs in the past three years, underscoring its mechanical robustness (Fig. S9). The superior mechanical properties of dry-PCL-SIPE are primarily attributed to the chemical grafting of LiHPSI onto the PVDF-CTFE backbone. This grafting enhances the polymer network's structural integrity, allowing it to resist deformation more effectively under stress. The covalent bonding promotes a more uniform stress distribution, resulting in increased Young's modulus and tensile strength. In contrast, dry-PC/L-DIPE relies solely on a physical blending approach, where stress is not efficiently transferred between the polymer matrix and dispersed phases. This phase incompatibility limits its mechanical performance. These findings demonstrate that chemical grafting significantly outperforms simple blending in enhancing mechanical properties. While the tensile strength of PCL-SIPE decreases to 1.68 MPa due to the liquid PC uptake, the break elongation increases by

approximately 16 times compared to the dry state (Fig. 1H). This observation suggests that the absorbed PC plasticizes the polymer matrix, improving its flexibility while reducing its ability to withstand higher tensile forces.

Thermal stability, a crucial factor in evaluating battery safety, was compared *via* conducting membrane heating and thermogravimetric analysis (TGA) tests. As shown in Fig. 1I, when heated to 220 °C, the dry-PCL-SIPE and dry-PC/L-DIPE exhibit minimal thermal shrinkage, suggesting its superiority over that of commercial separators. TGA was employed to further investigate the thermal stability and liquid uptake rate (Fig. S10 and Table S3). The dry-PCL-SIPE substantially delays the thermal lithium salt decomposition temperature from 246 °C to 331 °C, underscoring the vital role of chemical grafting in enhancing the thermal feature. As expected, incorporating the molecular transporter, PC, initiates lower onset decomposition temperature, predominantly due to its plasticizing effect reducing the crystallinity of copolymer, as revealed by the

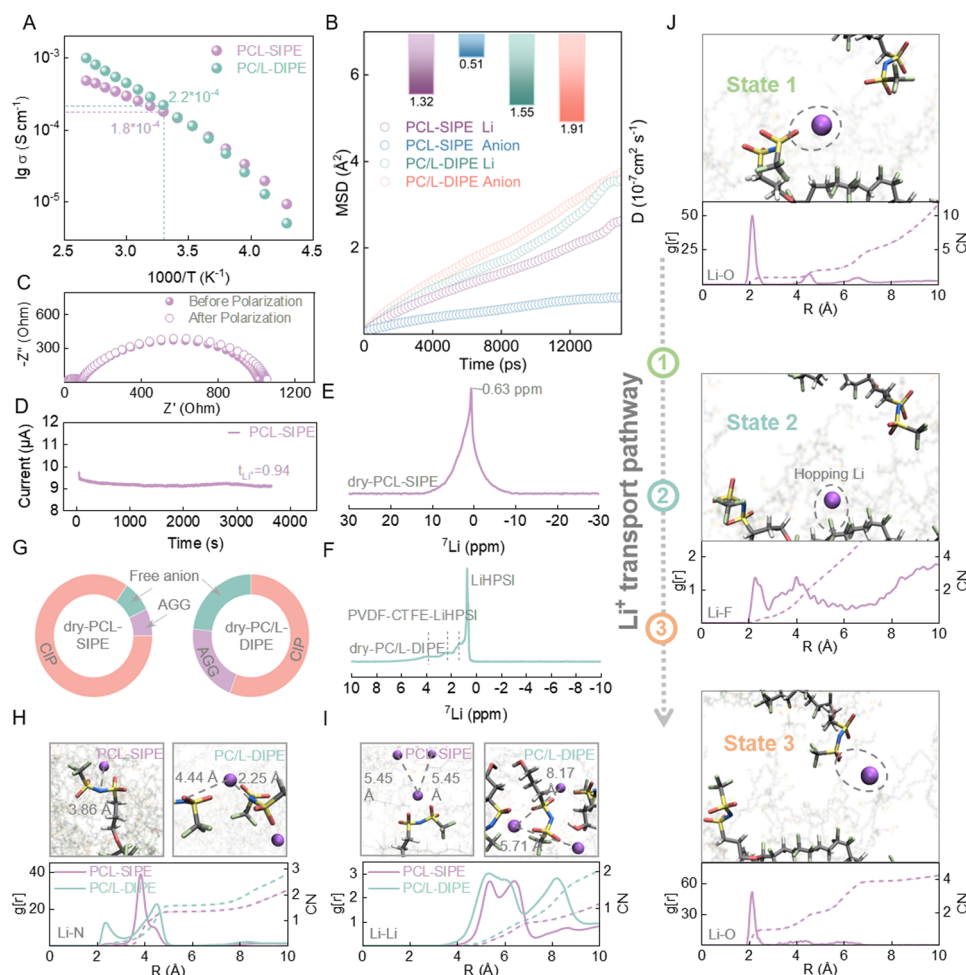


**Fig. 2** Investigation of Li-ion transport kinetics and mechanism. (A) Temperature-dependent ionic conductivities of PCL-SIPE and PC/L-DIPE (−40 to 100 °C). (B) MSD of PCL-SIPE and PC/L-DIPE. (C and D) AC impedance spectroscopy before and after polarization, and chronoamperometry curve before and after polarization for PCL-SIPE.  $^{7}\text{Li}$  NMR spectra of (E) dry-PCL-SIPE and (F) dry-PC/L-DIPE. (G) Contribution of the various Raman peaks relative to HPSI $^{-}$  anions in the spectrum of dry-PCL-SIPE and dry-PC/L-DIPE. (H) Li–N pair radial distribution functions in the PCL-SIPE and PC/L-DIPE systems, along with their snapshots. (I) Li–Li pair radial distribution functions in the PCL-SIPE and PC/L-DIPE systems, along with their snapshots. (J) Snapshots of the lithium transport pathway in PCL-SIPE (C: grey; H: white; O: red; N: blue; S: yellow; F: green; Li: purple).



sharply decreased glass transition temperature (Fig. S11 and S12). The initial weight loss of PCL-SIPE and PC/L-DIPE occurs between 107–174 °C and 128–221 °C, respectively, and can be assigned to the evaporation of PC. The weight loss of PC in PCL-SIPE and PC/L-DIPE is consistent with the liquid uptake ratio calculated using eqn (S1). The qualitative flammability assessment of dry-PCL-SIPE, PCL-SIPE and Celgard 2325 separator (polypropylene–polyethylene–polypropylene, PP–PE–PP) with 1 M LiPF<sub>6</sub> in EC/DEC/DMC are shown in Videos S1–S3. The results show that the dry-PCL-SIPE, representing a fully solid-state electrolyte, exhibits a self-extinguishing behavior when exposed to an open flame, indicating its excellent flame retardancy (Video S1). In contrast, the PC-containing PCL-SIPE membrane sustains combustion until the PC is consumed (Video S2), while the commercial liquid electrolyte system (1 M LiPF<sub>6</sub> in EC/DEC/DMC) burns violently and completely (Video S3), highlighting the severe safety risks associated with liquid electrolytes.

### Exploration of ion transport mechanisms in PCL-SIPE

The temperature-dependent ionic conductivities of PCL-SIPE and PC/L-DIPE were measured between –40 °C and 100 °C. A typical Vogel–Tammann–Fulcher model is evidenced in Fig. 2A, indicating solvent-coordinated Li<sup>+</sup> cation transport behaviour. At 30 °C, the ionic conductivity of PCL-SIPE and PC/L-DIPE is  $1.8 \times 10^{-4}$  S cm<sup>–1</sup> and  $2.2 \times 10^{-4}$  S cm<sup>–1</sup>, respectively. Notably, PCL-SIPE exhibits superior advantages at lower temperature, as the immobilization of anions effectively suppresses ion pairing and prevents the mobility decline of bulky anions. Molecular dynamics (MD) simulations provide further insights into the transport mechanism and solvation structure (Fig. 2B). The mean-squared displacement (MSD) analysis reveals diffusion coefficients at 400 K of  $1.3 \times 10^{-7}$  cm<sup>2</sup> s<sup>–1</sup> for Li<sup>+</sup> and  $0.5 \times 10^{-7}$  cm<sup>2</sup> s<sup>–1</sup> for anions in the PCL-SIPE system. While for the PC/L-DIPE system, the diffusion coefficients are  $1.5 \times 10^{-7}$  cm<sup>2</sup> s<sup>–1</sup> for Li<sup>+</sup> and  $1.9 \times 10^{-7}$  cm<sup>2</sup> s<sup>–1</sup> for anions, slightly higher than those of the PCL-SIPE system. The estimated ionic conductivities from MD simulations,  $1.55 \times 10^{-3}$  S cm<sup>–1</sup> for PCL-SIPE and  $2.98 \times 10^{-3}$  S cm<sup>–1</sup> for PC/L-DIPE, align well with experimental results, validating the model and computational methodology. Besides, the  $t_{\text{Li}^+}$  reflects the contribution lithium-ions to the overall ionic conductivity.<sup>30</sup> As shown in Fig. 2C and D (Fig. S13A and B) and eqn (S3), the  $t_{\text{Li}^+}$  values for PCL-SIPE and PC/L-DIPE are 0.94 and 0.39, respectively (calculated as detailed in Table S4). This indicates that PCL-SIPE exhibits typical single-ion conducting properties. The MSD analysis further supports these findings: in the PCL-SIPE system, Li<sup>+</sup> ions move considerably faster than the anions, whereas in the PC/L-DIPE system, the anions exhibit higher mobility. Although the ionic conductivity of PCL-SIPE is slightly lower than that of PC/L-DIPE, the high  $t_{\text{Li}^+}$  of 0.94 for PCL-SIPE suggests that Li<sup>+</sup> transport dominates, which helps reduce internal concentration gradients and inhibits lithium dendrite growth.<sup>31</sup>

Solid-state <sup>7</sup>Li NMR spectroscopy was employed to further investigate the local environment and transport mechanism of lithium-ions in the electrolyte (Fig. 2E and F). Compared to the dry-PC/L-DIPE (0.73 ppm), the reduced chemical shift in the

dry-PCL-SIPE (0.63 ppm) indicates an increased electron cloud density around Li<sup>+</sup>, suggesting stronger Li<sup>+</sup>-anion interactions. This enhanced interaction, however, correlates with a comparatively lower Li<sup>+</sup> mobility,<sup>32</sup> consistent with previous literature.<sup>33</sup> In addition to the 0.73 ppm peak attributed to LiHPSI, three additional peaks corresponding to PVDF-CTFE interacting with LiHPSI in PC/L-DIPE are observed at 1.38, 2.41, and 3.95 ppm, respectively.

Raman spectroscopy was conducted to investigate the anion coordination, revealing that Li-ions in the dry-PC/L-DIPE are more extensively aggregated than in the dry-PCL-SIPE (Fig. 2G and Fig. S14). The radial distribution function (RDF) of Li and N atoms (Fig. 2H) further supports this observation. In the PCL-SIPE system, a single peak is observed due to the presence of only one nitrogen atom per side chain, with a coordination number of 1.4, indicating the single-ion conducting nature of the copolymer. In contrast, PC/L-DIPE shows two distinct peaks, indicating the existence of aggregates (AGGs) formed by multiple anions interacting with a Li-ion, as shown in the corresponding snapshot, and multiple Li-ions interacting with an anion for the overall charge balance. The microscopic distribution of Li<sup>+</sup> in the PCL-SIPE and PC/L-DIPE systems was evaluated using the Li–Li RDF (Fig. 2I). The PCL-SIPE exhibits only two relatively shorter and narrower peaks, indicating a more uniform distribution of Li-ions. In contrast, the PC/L-DIPE displays two broader peaks, indicating random Li–Li interactions and confirming the existence of AGGs. This is consistent with the results from Raman spectroscopy analysis. The interaction force of Li<sup>+</sup>-anion and Li<sup>+</sup>-PC in the PCL-SIPE and PC/L-DIPE systems was evaluated using the Li–O RDF (Fig. S15 and S16). The coordination number of the PCL-SIPE system is 2.1, while that of the PC/L-DIPE system is 1.6, indicating the binding between lithium-ions and oxygen is more robust in the PCL-SIPE, with a reduced number of free Li-ions. Nevertheless, there is essentially no distinction between the Li<sup>+</sup>-O (PC) RDF of the two systems, thus, PC itself lacks analytical significance.

To further elucidate the Li<sup>+</sup> transport mechanisms, the hopping events alongside the coordination environment were investigated, which are illustrated in Fig. 2J. In the initial stage, the Li-ion is predominantly coordinated with the anchored anion, maintaining a Li–O distance of 2.0 Å (state 1). Subsequently, the Li-ion hops to state 2 by dissociating from the anion's oxygen and hopping to the PVDF-CTFE backbone. In the third step, the Li<sup>+</sup> ion hops to another, nearby, anchored anion forming a lithium–oxygen coordination bond with a Li–O distance of 2.0 Å (state 3), overall resulting in its migration along the alternating copolymer structure. This analysis highlights the complex dynamics of Li<sup>+</sup> transport within the system.

### Investigation of the electrochemical behavior of PCL-SIPE and PC/L-DIPE

The electrochemical stability of PCL-SIPE and PC/L-DIPE was evaluated *via* performing linear sweep voltammetry and cyclic voltammetry (CV) measurements. The electrochemical stability window of PCL-SIPE is found to be about 4.7 V (Fig. 3A), which is substantially higher than that of the PC/L-DIPE (*ca.*, 3.15 V,



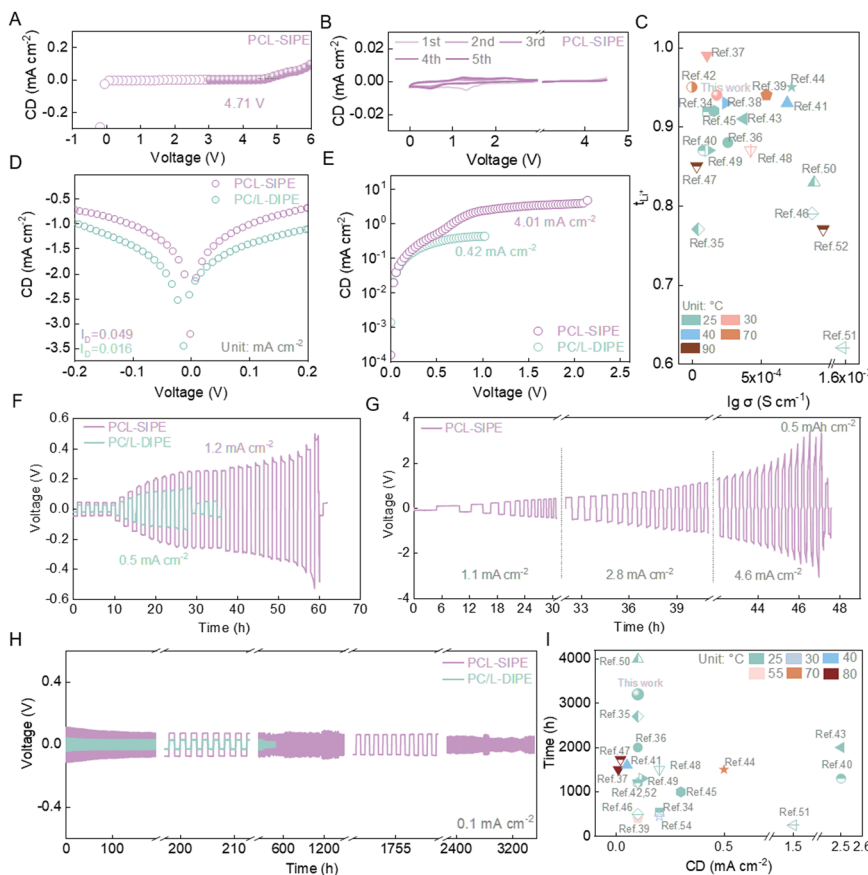


Fig. 3 Electrochemical performance of polymer electrolytes. (A) Electrochemical stability window of the PCL-SIPE (sweep rate:  $0.2 \text{ mV s}^{-1}$ ). (B) Reduction (0.0–3.0 V) and oxidation (3.0–4.5 V) stability of the PCL-SIPE ( $\text{Li}||\text{SS}$  cells, sweep rate:  $0.2 \text{ mV s}^{-1}$ ). (C) Comparison of  $t_{\text{Li}^+}$  and ionic conductivity with other reported SIPEs in the past three years. (D) Tafel curves of PCL-SIPE and PC/L-DIPE. (E) Limiting current density of PCL-SIPE and PC/L-DIPE. (F) CCD of the  $\text{Li}|\text{PCL-SIPE}|\text{Li}$  and  $\text{Li}|\text{PC/L-DIPE}|\text{Li}$  symmetric cells with a stripping-plating period of 1 h. (G) CCD of the  $\text{Li}|\text{PCL-SIPE}|\text{Li}$  symmetric cells with a fixed capacity of  $0.5 \text{ mAh cm}^{-2}$ . (H) Cycling performance of the  $\text{Li}|\text{PCL-SIPE}|\text{Li}$  and  $\text{Li}|\text{PC/L-DIPE}|\text{Li}$  symmetric cells at a current density of  $0.1 \text{ mA cm}^{-2}$ . (I) Comparison of the cycling performance with other reported SIPEs in the past three years.

Fig. S17), due to the physical blending of lower molecular weight LiHPSI with PVDF-CTFE, which is more prone to oxidative decomposition at high voltage. The reduction peak of PCL-SIPE located at approximately 1.3 V in the CV profiles recorded within the voltage range of 0.0–3.0 V (Fig. 3B) is attributed to the reductive decomposition of PC.<sup>26</sup> Its disappearance in the following cycles implies that the initial decomposition of PC induces a stable electrode|electrolyte interface and interphase. Conversely, the PCL-SIPE exhibits remarkable stability against oxidation, as indicated by the extremely low current density recorded in the range of 3–4.5 V. In stark contrast, the PC/L-DIPE exhibits poor stability toward both reduction and oxidation (Fig. S18 and S19). This improvement highlights the significance of covalently anchoring the anions onto the copolymer chains.

The effective lithium-ion conductivities of PCL-SIPE and PC/L-DIPE were calculated to be  $1.69$  and  $0.86 \text{ mS cm}^{-1}$  ( $30^\circ\text{C}$ ), respectively. The PCL-SIPE exhibits conductivity values comparable to those reported in the past three years<sup>34–52</sup> (see Fig. 3C and Table S5). Additionally, the electronic conductivity of PCL-SIPE decreases by a factor of 5 (from  $1.4 \times 10^{-9} \text{ S cm}^{-1}$

to  $2.7 \times 10^{-10} \text{ S cm}^{-1}$ ) compared with the one of PC/L-DIPE (Fig. S20). Tafel plots were constructed to analyse the electrochemical reaction kinetics of the two polymer electrolytes (Fig. 3D). The PCL-SIPE exhibits higher exchange current densities ( $I_0$ ) and lower polarization, promoting rapid charge transfer and faster kinetics. Furthermore, as shown in Fig. 3E, the limiting current density is increased nearly by a factor of 10, *i.e.*,  $4.01 \text{ mA cm}^{-2}$  (PCL-SIPE) vs.  $0.42 \text{ mA cm}^{-2}$  (PC/L-DIPE). In addition, the concentration gradient of PC/L-DIPE caused by the increased voltage makes the plateau different from that of the PCL-SIPE.<sup>53</sup> These findings corroborate the significantly enhanced kinetic property of PCL-SIPEs.

To assess the stability of the  $\text{Li}|\text{electrolyte}$  interface and the effectiveness in inhibiting lithium dendrite formation, lithium stripping-plating experiments were conducted in  $\text{Li}||\text{Li}$  cells at  $25^\circ\text{C}$ . The PCL-SIPE achieves higher critical current densities (CCD), *i.e.*,  $1.2$  vs.  $0.5 \text{ mA cm}^{-2}$  in the constant-time mode (Fig. 3F), and  $4.6$  vs.  $0.3 \text{ mA cm}^{-2}$  in the constant-capacity mode (Fig. 3G and Fig. S21). Collectively, these results indicate that PCL-SIPE is capable of preventing lithium dendrite formation and ensuring sufficient kinetics even under high-power



conditions. Subsequently, Li|PCL-SIPE|Li and Li|PC/L-DIPE|Li cells were subjected to long-term galvanostatic lithium stripping and plating test at  $0.1 \text{ mA cm}^{-2}$  (Fig. 3H). Although the Li|PC/L-DIPE|Li cell exhibits a lower overpotential, a short circuit occurs after 323 h of cycling. In contrast, the Li|PCL-SIPE|Li cell demonstrates relatively constant voltage, reaching 0.04 V after 3200 h of cycling, indicating the excellent interfacial stability and effective inhibition of lithium dendrite formation. This underscores the outstanding cyclability of PCL-SIPE, even when compared to recent studies on SIPEs (Fig. 3I and Table S6).<sup>34–37,39–52,54</sup>

### Uncovering the evolution of interface and interphase in symmetric Li||Li cells

In order to further clarify the electrochemical behaviour of PCL-SIPE and PC/L-DIPE, impedance measurements were performed on Li|PCL-SIPE|Li and Li|PC/L-DIPE|Li cells upon cycling. By comparing the Nyquist plots, it is observed that the high-frequency impedance contributes to the dominant overall impedance in the PC/L-DIPE system (Fig. 4A and B).

Although the Nyquist plots effectively reveal differences between the two electrolytes in both the high and low frequency regions, they offer limited resolution in deconvoluting specific impedance sources. Therefore, distribution of relaxation times (DRT) analysis was employed to decouple dynamic behaviours and investigate the underlying electrochemical mechanisms (Fig. 4C–F). To perform a detailed numerical analysis, the impedance data were fitted to extract specific impedance values

associated with various dynamic behaviours (see Fig. 4G–I and Table S7). The equivalent circuit model applied for fitting the DRT results is illustrated in Fig. S22. In the PCL-SIPE system, P1 ( $10^{-7} \text{ s}$ ) reflects the  $\text{Li}^+$  transport channels formed by PC and copolymer, which is closely related to the ionic conductivity of the electrolytes.<sup>55</sup> In contrast, the presence of PC in the PC/L-DIPE system facilitates the solvation of free LiHPSI salts, thereby rendering the system liquid-electrolyte-dominated. To clarify the  $\text{Li}^+$  transport mechanism in PC/L-DIPE, we conducted theoretical calculations of  $\text{Li}^+$  RDFs in PC solvent and the PVDF-CTFE polymer matrix (Fig. S23). Results show negligible coordination between PVDF-CTFE and  $\text{Li}^+$ , with extremely weak RDF peaks and near-zero coordination numbers, indicating that  $\text{Li}^+$  transport along the polymer backbone is not dominant. Therefore, in the PC/L-DIPE system, the P1 peak ( $10^{-7} \text{ s}$ ) corresponds to  $\text{Li}^+$  transport pathways primarily governed by liquid-phase conduction. This process is consistent with the overall ionic conductivity of the electrolyte. The P2 peak ( $10^{-5} \text{ s}$  to  $10^{-6} \text{ s}$ ) may be attributed to interfacial impedance potentially arising from the direct contact between undissociated solid-phase lithium salts and the polymer matrix. P3 ( $10^{-4} \text{ s}$  to  $10^{-5} \text{ s}$ ) indicates the evolution of the SEI during  $\text{Li}^+$  deposition.<sup>56</sup> The more stable SEI layer in PCL-SIPE with respect to the PC/L-DIPE system, contributes to the superior cycling performance of the former electrolyte. P4 ( $10^{-4} \text{ s}$  to  $10^{-3} \text{ s}$ ) represents the charge transfer process.  $R_{ct}$  in PCL-SIPE is higher than that in PC/L-DIPE during the whole cycling process. This behaviour is ascribed to the effective wetting of the electrode surface by solvent molecules in the PC/L-DIPE

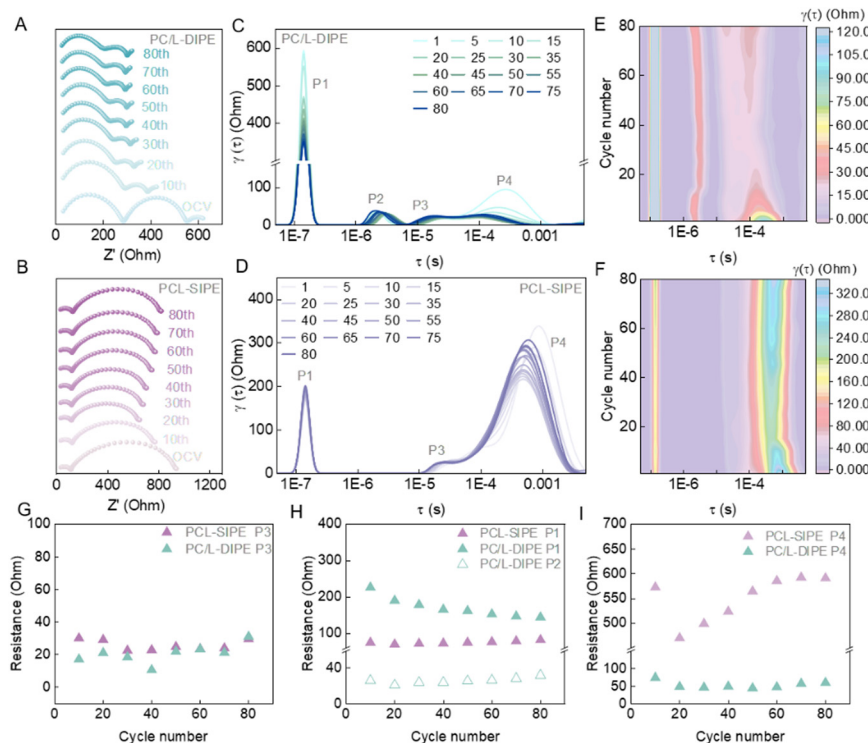


Fig. 4 Distribution of relaxation times analyses of polymer electrolytes. (A and B) Nyquist plots of PC/L-DIPE and PCL-SIPE. (C and D) DRT analysis of the EIS results of PC/L-DIPE and PCL-SIPE. (E and F) DRT contour plots of PC/L-DIPE and PCL-SIPE. (G–I) Evolution of P1, P2, P3 and P4 resistances (after normalization) of PC/L-DIPE and PCL-SIPE.



system, which enables the formation of continuous and uniform interfacial contact, thereby promoting charge transfer.

To study the surface morphology of the cycled lithium electrode,  $\text{Li}||\text{Li}$  cells were assembled, and lithium stripping-plating experiments were conducted at a current density of  $0.2 \text{ mA cm}^{-2}$ . The voltage profiles are shown in Fig. S24. The surface and cross-sectional morphologies of the pristine lithium anode are displayed in Fig. S25. After cycling, the surface and cross-sectional morphologies, as well as the EDS mapping were also examined. Through comparison, both cycled Li electrodes present rougher surfaces, with respect to the pristine Li metal. Nevertheless, the lithium anodes cycled with PC/L-DIPE (Fig. S27) display a noticeably rougher surface, contrasting sharply with the smooth surface of those cycled with PCL-SIPE (Fig. S26). Notably, no mossy or dendritic lithium growth is seen in  $\text{Li}|\text{PCL-SIPE}|\text{Li}$  cells after cycling. Cross-sectional morphology analysis further reveals that the reactive/dead lithium layer on the cycled Li electrode recovered from  $\text{Li}|\text{PCL-SIPE}|\text{Li}$  cells is remarkably thin, indicating that PCL-SIPE facilitates more uniform lithium deposition. Additionally, the minor EDS mapping signals of cycled Li

electrode recovered from Li|PCL-SIPE|Li cells further corroborate the significantly mitigated interfacial side reactions.

To investigate the SEI composition, X-ray photoelectron spectroscopy (XPS) was performed (Fig. 5A and Fig. S28). From the high-resolution F 1s XP spectra, it is seen that the SEI layer of the PCL-SIPE system contains higher amounts of LiF than that of the PC/L-DIPE system. LiF can regulate the  $\text{Li}^+$  flux and promote the uniform deposition of  $\text{Li}^+$ ,<sup>57</sup> thus improving the cycle life of  $\text{Li}|\text{PCL-SIPE}|\text{Li}$  cells. The high-resolution S 2p and N 1s XP spectra reveal that the SEI layer of the PC/L-DIPE system contains higher amounts of N and S elements, attributed to increased  $\text{HPST}^-$  decomposition facilitated by the free anions reaching the electrode|electrolyte interface. The high-resolution C 1s, O 1s, Li 1s and Cl 2p XP spectra of PCL-SIPE and PC/L-DIPE are shown in Fig. S28. Notably, the LiCl peak at 56.2 eV in the Li 1s spectrum of the PC/L-DIPE system indicates the decomposition of PVDF-CTFE.

Time-of-flight secondary ion mass spectrometry (ToF-SIMS) was carried out to characterize the interphases at a time of 1000 s, with a main focus on the distribution of molecular

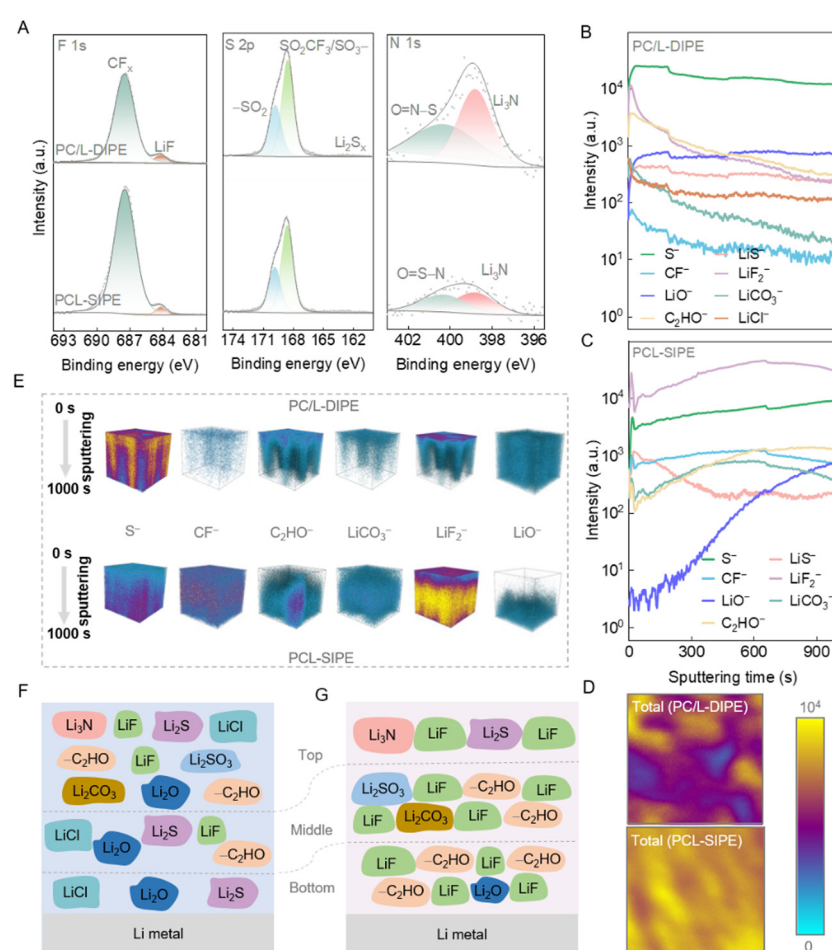


**Fig. 5** Examination of SEI compositions of cycled Li metal recovered from Li|PC/L-DIPE|Li and Li|PCL-SIPE|Li cells. (A) F 1s, S 2p, N 1s *ex situ* XP spectra. (B and C) Depth profiling of representative SEI components. (D) Comparative 2D rendered images of overall component distribution in the SEI layer. (E) Comparative 3D rendered images of representative sputtered secondary-ion fragments of SEI layers. (F and G) Schematic representation of the SEI compositions in the PC/L-DIPE and PCL-SIPE systems.

fragments and functional groups to analyse the spatial distribution of SEI components. Depth profiling results of representative secondary ion fragments are shown in Fig. 5B and C, and Fig. S29. The sulfur (S) content in the SEI layer of the PC/L-DIPE system is remarkably higher than that of the PCL-SIPE system, indicating intensive lithium salt decomposition in the former, which is in agreement with the conclusions drawn from XPS and the possibility for the free anion to reach the electrode interface. The PC/L-DIPE shows considerably higher content of  $-\text{LiO}$  with rather uniform spatial distribution within the SEI layer. It is reported that  $\text{Li}_2\text{O}$  can contribute to robust mechanical strength and enhanced interfacial kinetics.<sup>58</sup> However, the favored LiF mainly accumulates on the surface of the SEI layer, hindering effective and uniform  $\text{Li}^+$  transport to the lithium metal. In stark contrast, the PCL-SIPE system exhibits much lower overall lithium salt decomposition and, moreover, a high content of LiF and  $\text{Li}_2\text{O}$  in the bottom SEI layer. This could be assigned to the more complete decomposition of anions bound to the co-polymer and residing nearby the electrode interface, concomitantly with a higher proportion of  $-\text{CF}$  and lower  $-\text{CF}_3$ . Additionally, the organic component,  $-\text{C}_2\text{HO}$ , gradually decreases with increasing sputtering depth in the SEI layer of the PC/L-DIPE system, whereas an inverse trend is observed in the PCL-SIPE system. This suggests that PC decomposition intensifies in the PC/L-SIPE system, but diminishes in the PCL-SIPE system as cycling progresses.

Fig. 5D compares the 2D rendered overall distribution of total secondary ion fragments between PC/L-DIPE and PCL-SIPE systems. In the PC/L-DIPE system, the SEI components show uneven distribution due to poor compatibility between the lithium salt and the PVDF-CTFE interface, and moreover, the inhomogeneous Li deposition over cycling. Furthermore, the corresponding 3D rendering graphs (Fig. 5E and Fig. S30) more distinctly provide a visual representation of the spatial distribution of primary SEI components. Based on the above results, the SEI models are depicted in Fig. 5F and G, respectively. Compared with the SEI layer in the PC/L-DIPE system, the one in the PCL-SIPE system is denser, richer in LiF, and contains a higher content of organic components. The organic matrix mitigates interfacial stress and accommodates volume changes during cycling, thus preventing cracking or detachment of the SEI. In contrast, inorganic species such as  $\text{Li}_2\text{O}$  and LiF serve to reinforce mechanical robustness and contribute to high interfacial ionic conductivity. The LiF/ $\text{Li}_2\text{CO}_3$  interfacial phases can further promote the diffusion of  $\text{Li}^+$  and prevent the decomposition of the electrolyte.<sup>49</sup> This cooperative organic–inorganic architecture facilitates stable interfacial dynamics and contributes to the prolonged cycling stability of Li metal anodes. In contrast, the absence of LiF at the bottom of the SEI layer in the PC/L-DIPE system leads to the non-uniform deposition of  $\text{Li}^+$ , which will reduce the cycle life of the cells.

### Evaluation of the electrochemical performances in full-cell configurations

To assess the performance in full-cells, an LFP cathode with a mass-loading of  $2.0 \text{ mg cm}^{-2}$  was paired with PCL-SIPE and

PC/L-DIPE. As shown in Fig. 6A and Fig. S31, the discharge capacities of the  $\text{Li}|\text{PCL-SIPE}|\text{LFP}$  coin full-cells are always higher than those of the  $\text{Li}|\text{PC/L-DIPE}|\text{LFP}$  coin full-cells at all C-rates ranging from 0.1 to 3.0C (164.2 to 74.1  $\text{mAh g}^{-1}$ ). In contrast, no capacity can be delivered in the case of the  $\text{Li}|\text{PC/L-DIPE}|\text{LFP}$  coin full-cells at 2.0C (Fig. S32). It is worth noting that when the C-rate returns from 3.0C to 0.1C, the  $\text{Li}|\text{PCL-SIPE}|\text{LFP}$  coin full-cells exhibit superior reversibility *via* fully recovering their original capacities. In comparison, strong capacity decay is observed in the  $\text{Li}|\text{PC/L-DIPE}|\text{LFP}$  coin full-cells at a given C-rate. This excellent rate capability is attributed to the fast kinetics of PCL-SIPE, supported by its high effective ionic conductivity, limiting current density, and critical current density, along with optimized SEI composition, ensuring ultra-high stability against lithium metal. Subsequently, the cycling stability of  $\text{Li}|\text{PCL-SIPE}|\text{LFP}$  coin full-cells is evaluated at 0.5C and 1.0C (Fig. 6B). Capacity retention of 88.50% and 53.36% was achieved after 500 cycles at 0.5C and 1.0C (the average Coulombic efficiencies are 99.94% and 99.96%, respectively). The specific discharge capacity initially increases over the first few cycles before stabilizing. In contrast, the  $\text{Li}|\text{PC/L-DIPE}|\text{LFP}$  coin full-cells exhibited a capacity retention of 36.41% and an average CE of 49.59% after 77 cycles at 0.1C (Fig. S33). Compared to the  $\text{Li}|\text{PCL-SIPE}|\text{LFP}$  coin full-cells, the  $\text{Li}|\text{PC/L-DIPE}|\text{LFP}$  coin full-cells exhibit lower average Coulombic efficiencies (CE), primarily due to anion migration in the PC/L-DIPE system, which induces concentration polarization and interfacial side reactions, thereby leading to irreversible lithium plating/stripping. A comparison of full-cell performance of PCL-SIPE with recent studies on SIPEs from the past three years (Fig. 6C and Table S8) reveals that PCL-SIPE offers a significant advantage in cycle life.<sup>34–40,42–52,54</sup>

In order to understand the reasons behind the significantly boosted cycling performance, EIS measurements of a  $\text{Li}|\text{PCL-SIPE}|\text{LFP}$  full-cell ( $2 \text{ mg cm}^{-2}$ , 1.0C,  $25^\circ\text{C}$ , 200 cycles) were performed through recording the Nyquist plots every 10 cycles. As shown in Fig. S34, the overall impedance remains rather stable after 20 cycles, indicating extremely stable interphases at both the  $\text{Li}|\text{PCL-SIPE}$  and  $\text{LFP}|\text{PCL-SIPE}$  interfaces. It is worth mentioning that the 200 cycles of dis-/charge voltage profiles of the  $\text{Li}|\text{PCL-SIPE}|\text{LFP}$  cell almost coincide (Fig. S35), an indication of excellent stability with minimized polarization. With the increase of cycle numbers, the stabilized polarization voltage gap indicates that the electrochemical reactions inside the battery gradually reach equilibrium. Furthermore, *ex situ* SEM and EDS analyses of cycled Li electrodes were conducted, as demonstrated in Fig. S36 and S37. Notably, no obvious dendrites are observed on the surface of the lithium metal after cycling, and the elements in the EDS mapping are evenly distributed, with no visible protrusions or cracks. Moreover, the cycled lithium metal maintains a dense structure. This suggests that the PCL-SIPE system effectively inhibits the growth of lithium dendrites during cycling.

### Exploration of full-cell performance under exertive scenarios

Given the excellent cycling stability of  $\text{Li}|\text{PCL-SIPE}|\text{LFP}$  coin full-cells, further efforts were dedicated to exploring the cycling



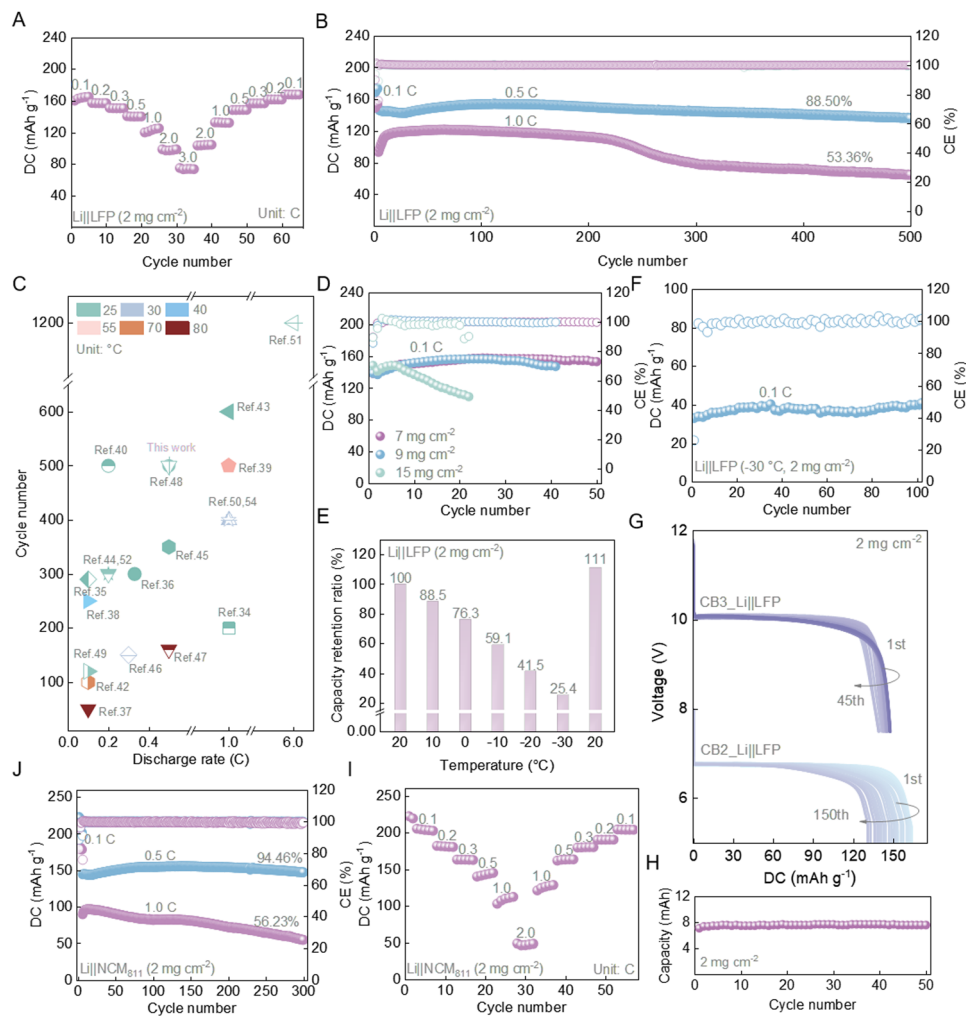


**Fig. 6** Electrochemical performances of PCL-SIPE in full-cells. (A) Rate capability of  $\text{Li}|\text{PCL-SIPE}| \text{LFP}$  coin full-cells. (B) Galvanostatic cycling of  $\text{Li}|\text{PCL-SIPE}| \text{LFP}$  coin full-cells at a C-rate of 0.5C (in blue) and 1C (in purple) after three formation cycles at 0.1C. (C) Comparison of galvanostatic cycling life with other reported full-cells incorporating SIPEs in the past three years. (D) Galvanostatic cycling stability at 0.1C with varying areal mass-loadings of 7.0, 9.0, and 15.0  $\text{mg cm}^{-2}$ . (E) Capacity retention ratios of  $\text{Li}|\text{PCL-SIPE}| \text{LFP}$  coin full-cells at different temperatures (the discharge specific capacity at 20  $^{\circ}\text{C}$  is defined as 100% capacity retention ratio). (F) Galvanostatic cycling of  $\text{Li}|\text{PCL-SIPE}| \text{LFP}$  coin full-cells (0.1C, -30  $^{\circ}\text{C}$ ). (G) Discharge voltage profiles of the bilayer (5–8 V) and trilayer (7.5–12 V) bipolar stacking cells (0.1C). (H) Cycling performance of the  $\text{Li}|\text{PCL-SIPE}| \text{LFP}$  pouch full-cell at 0.1C with an areal mass-loading of 2.0  $\text{mg cm}^{-2}$ . (I) Rate capability of  $\text{Li}|\text{PCL-SIPE}| \text{NCM}_{811}$  coin full-cells. (J) Galvanostatic cycling performance of  $\text{Li}|\text{PCL-SIPE}| \text{NCM}_{811}$  coin full-cells with a C-rate of 0.5C (in blue) and 1C (in purple) after three formation cycles at 0.1C.

stability with gradually increasing LFP mass-loadings. At 0.1C, there's only a minor difference in delivered capacity when increasing the mass of LFP from 7.0 to 9.0  $\text{mg cm}^{-2}$  and further to 15.0  $\text{mg cm}^{-2}$  (Fig. 6D). The  $\text{Li}|\text{PCL-SIPE}| \text{LFP}$  coin full-cells with an LFP mass-loading of 7.0  $\text{mg cm}^{-2}$  still achieve impressive cyclability for over 50 cycles with a capacity retention of 97.02% and an average CE of 99.84%. Increasing the mass of LFP to 15.0  $\text{mg cm}^{-2}$ , the  $\text{Li}|\text{PCL-SIPE}| \text{LFP}$  coin full-cells are still capable of maintaining more than 10 stable cycles, with an average CE of 98.19%. The reduced average CE at a high mass-loading can be attributed to sluggish ion transport and aggravated side reactions associated.

Considering the salient advantages of PCL-SIPE in terms of ionic conductivity in low-temperature regions, fresh full-cells were subjected to galvanostatic cycling at 0.1C under various

temperature conditions (Fig. 6E and Fig. S38). Between -30  $^{\circ}\text{C}$  and 20  $^{\circ}\text{C}$ , the  $\text{Li}|\text{PCL-SIPE}| \text{LFP}$  coin full-cells exhibit a reversible discharge capacity of 130.5  $\text{mAh g}^{-1}$  (20  $^{\circ}\text{C}$ ), 115.4  $\text{mAh g}^{-1}$  (10  $^{\circ}\text{C}$ ), 99.6  $\text{mAh g}^{-1}$  (0  $^{\circ}\text{C}$ ), 77.1  $\text{mAh g}^{-1}$  (-10  $^{\circ}\text{C}$ ), 54.2  $\text{mAh g}^{-1}$  (-20  $^{\circ}\text{C}$ ) and 33.2  $\text{mAh g}^{-1}$  (-30  $^{\circ}\text{C}$ ), respectively. Notably, at -30  $^{\circ}\text{C}$ , the cell retains 25.4% of the capacity achieved at 20  $^{\circ}\text{C}$ . Subsequently, the galvanostatic cycling stability of  $\text{Li}|\text{PCL-SIPE}| \text{LFP}$  coin full-cells at -30  $^{\circ}\text{C}$  is evaluated (Fig. 6F). Upon 100 consecutive cycles, the cells exhibited a capacity retention of 98.51% and an average CE of 98.78%, demonstrating its promising potential towards applications in low temperature environments.

To demonstrate the feasibility of implementing bipolar stacking cells with PCL-SIPE, “proof-of-concept” bilayer (SS|Li|PCL-SIPE|LFP|SS|Li|PCL-SIPE|LFP) coin full-cells (SS: stainless

steel), denoted as CB2\_Li||LFP, and trilayer (SS|Li|PCL-SIPE|LFP|SS|Li|PCL-SIPE|LFP|SS|Li|PCL-SIPE|LFP) coin full-cells, denoted as CB3\_Li||LFP, were assembled. The open-circuit voltages of fresh CB2\_Li||LFP and CB3\_Li||LFP coin full-cells are 6.7 V and 10.1 V (Fig. S39), respectively. Fig. 6G and Fig. S40 display the discharge profiles of CB2\_Li||LFP and CB3\_Li||LFP coin full-cells. At 0.1C, the CB2\_Li||LFP coin full-cells deliver an initial specific discharge capacity of 154.3  $\text{mAh g}^{-1}$  between 8.0 V and 5.0 V. Upon cycling, the capacity initially increases and then gradually stabilizes at 164.7  $\text{mAh g}^{-1}$ , followed by a mild decreasing trend above 50 cycles. Impressively, to the best of our knowledge, the CB2\_Li||LFP coin full-cells obtain the best cycling performance *via* retaining 80.0% of the maximum capacity after 150 cycles, along with an average CE of 99.65%. Furthermore, in the voltage range of 12.0–7.5 V, the CB3\_Li||LFP coin full-cells deliver an initial specific discharge capacity of 139.4  $\text{mAh g}^{-1}$  which progressively increases to 147.5  $\text{mAh g}^{-1}$  after 45 cycles.

Li||LFP pouch full-cells (single layer pouch full-cell, PB1\_Li||LFP) were assembled to explore the practical potential of PCL-SIPE with various LFP mass-loadings (Fig. 6H and Fig. S41). The initial discharge capacities of the PB1\_Li||LFP pouch full-cell are 7.7  $\text{mAh}$  (2.0  $\text{mg cm}^{-2}$ ; Fig. 6H) and 15.0  $\text{mAh}$  (5.0  $\text{mg cm}^{-2}$ ; Fig. S40). The PB1\_Li||LFP pouch full-cell with lower LFP loading (2.0  $\text{mg cm}^{-2}$ ) are able to cycle more than 50 times with a capacity retention of 98.14% and average CE of 98.94%. The PB1\_Li||LFP pouch full-cell with higher LFP loading (5.0  $\text{mg cm}^{-2}$ ) deliver an initial capacity of 15.0  $\text{mAh}$ , and retain 69.61% of the maximum capacity after 40 cycles, with an average CE of 99.34%. To further demonstrate the feasibility of PCL-SIPE for high-energy-density applications, Cu|Li|PCL-SIPE|LFP|SS|Li|PCL-SIPE|LFP|SS|Li|PCL-SIPE|LFP pouch full-cells (PB3\_Li||LFP), composed of thin Li (40  $\mu\text{m}$ ), a high mass-loading LFP cathode (17  $\text{mg cm}^{-2}$ ) and thin PCL-SIPE film (28  $\mu\text{m}$ ), were assembled (Fig. S42). According to eqn (S5), this stacking configuration successfully achieved a high energy density of 245.88  $\text{Wh kg}^{-1}$  (Table S9). To assess the safety of PCL-SIPE, the PB1\_Li||LFP pouch full-cell was subjected to destructive tests (Fig. S43). Due to the flexibility of PCL-SIPE, the pouch full-cells continue to operate effectively after shearing and folding. Remarkably, even after being cut into pieces, the cells can still power a light-emitting diode panel. However, the Li|PP-PE-PP|LFP pouch full-cell stopped working after shearing, reinforcing the structural and safety advantages offered by the PCL-SIPE (Fig. S44).

Finally, the combination of PCL-SIPE with high-energy Ni-rich cathode materials was investigated in Li||NCM<sub>811</sub> coin full-cells. As shown in Fig. 6I, the Li||NCM<sub>811</sub> coin full-cells demonstrate a high reversible specific discharge capacity of 204.0  $\text{mAh g}^{-1}$  at 0.1C. Between 0.1C and 2.0C, the Li|PCL-SIPE|NCM<sub>811</sub> coin full-cells exhibit a reversible discharge capacity of 163.2  $\text{mAh g}^{-1}$  (0.3C), 142.7  $\text{mAh g}^{-1}$  (0.5C) and 46.0  $\text{mAh g}^{-1}$  (2.0C). After cycling at 2.0C, when the C-rate gradually reduces back to 0.1C, highly reversible capacities are delivered (Fig. 6I and Fig. S45). As shown in Fig. 6J, the Li||NCM<sub>811</sub> coin full-cells demonstrate excellent cycling performance at 0.5C and 1.0C over 300 cycles,

delivering average CEs of 99.84% and 99.54%, and capacity retention of 94.46% and 56.23%, respectively. The excellent cycling stability and rate capability of Li||NCM<sub>811</sub> cells highlight their potential for applications requiring both high energy and high power.

## Conclusions

We designed the PCL-SIPE with balanced ionic conductivity and mechanical properties by means of a Williamson reaction between LiHPSI, containing O–C–C bonds, and PVDF-CTFE, containing C–F bonds. Molecular dynamics simulations reveal the transport mechanism of lithium-ions in the PCL-SIPE, where F atoms in the co-polymer main chains facilitate  $\text{Li}^+$  transport between adjacent side chain groups. Compared with the dual-ion conductive counterpart (PC/L-DIPE), PCL-SIPE exhibits significantly better kinetic properties, higher tensile strength (20.65 *vs.* 5.65 MPa) and higher  $t_{\text{Li}^+}$  (0.94 *vs.* 0.39). These attributes are crucial in inhibiting the formation and growth of Li dendrites. *Ex situ* XPS and ToF-SIMS analyses demonstrate that PCL-SIPE induces the formation of a thermodynamically and kinetically favourable SEI consisting of a high amount of LiF and enriched  $\text{Li}_2\text{O}$  in the bottom layer, along with organic species that provide sufficient flexibility to accommodate the volume changes. As a result, the lithium stripping-plating lifetime of PCL-SIPE is substantially extended by approximately a factor of 10. This combination of properties enables excellent rate capability and cycling performance of Li||LFP and Li||NCM<sub>811</sub> coin full-cells, respectively, retaining 88.50% (500 cycles) and 94.46% (300 cycles) of their maximum capacity at 0.5C. Furthermore, the cells demonstrate outstanding performance when subjected to exertive conditions including elevated LFP mass-loadings (*ca.*, 7, 9, and 15  $\text{mg cm}^{-2}$ ), low temperatures ( $-30^\circ\text{C}$ ), multi-layer bipolar stacking (about 7 V and 10 V), and prototype pouch full-cells. Utilizing thin Li (40  $\mu\text{m}$ ), high mass-loading LFP cathode (17  $\text{mg cm}^{-2}$ ) and thin PCL-SIPE film (28  $\mu\text{m}$ ), the trilayer bipolar stacking pouch full-cell achieves an energy density of 245.88  $\text{Wh kg}^{-1}$ . Despite the incorporation of PC solvent, the Li|PCL-SIPE|LFP pouch full-cells' safety appears to be sufficiently demonstrated by their ability to operate under shearing, folding and cutting conditions. The developed strategy in this study is anticipated to be readily applicable for advanced high-energy and high-power LMBs, particularly in the fields of EVs and advanced air mobility applications, such as drones, and electric aircrafts.

## Author contributions

Yating Yu: conceptualization, data curation, formal analysis, investigation, visualization, writing – original draft, writing – review & editing. Sida Chen: data curation, formal analysis, investigation, validation, visualization, writing – original draft, writing – review & editing. Hai-Peng Liang: conceptualization, formal analysis, writing – review & editing. Ziqi Zhao: formal analysis, visualization, writing – original draft, writing – review & editing. Guangze Chu: data curation, investigation, writing – review & editing. Ziting



Zhi: data curation, investigation, writing – review & editing. Xian-Ao Li: visualization, writing – review & editing. Cheng Li: investigation, writing – review & editing. Ruixin Li: investigation, writing – review & editing. Youzhi Xu: funding acquisition, supervision, writing – review & editing. Xin Liu: funding acquisition, investigation, writing – review & editing. Minghua Chen: funding acquisition, writing – review & editing. Stefano Passerini: conceptualization, funding acquisition, supervision, writing – review & editing. Zhen Chen: conceptualization, formal analysis, funding acquisition, project administration, supervision, writing – review & editing. Yating Yu and Sida Chen contributed equally to this work.

## Conflicts of interest

There are no conflicts to declare.

## Data availability

All data supporting the findings of this study are included in the manuscript and the SI, or are available from the corresponding author upon reasonable request.

Supplementary information is available. See DOI: <https://doi.org/10.1039/d5ee02503f>

## Acknowledgements

This work is supported by the National Natural Science Foundation of China (Grant No. 52277215, 52307237, 22201064, and 22471060), the China Postdoctoral Science Foundation (No. 2023M730884), and the Postdoctoral Science Foundation of Heilongjiang Province of China (LBH. Z23024). S. P. acknowledges the basic funding from the Helmholtz Association and the Austrian Institute of Technology.

## Notes and references

- 1 H. Wan, J. Xu and C. Wang, *Nat. Rev. Chem.*, 2024, **8**, 30–44.
- 2 M. S. Whittingham, *Science*, 1976, **192**, 1126–1127.
- 3 Y. Wu, Z. Chen, K. Shi, Y. Wang, X.-A. Li, Z. Zhao, Q. Zhuang, J. Wang and M. Chen, *Energy Environ. Sci.*, 2025, **18**, 2817–2825.
- 4 X. Zhang, Q. Su, G. Du, B. Xu, S. Wang, Z. Chen, L. Wang, W. Huang and H. Pang, *Angew. Chem., Int. Ed.*, 2023, **62**, e202304947.
- 5 P. Wang, H. Li, N. Li, J. Sun, F. Xu, X. Tian and X. Shi, *Adv. Funct. Mater.*, 2025, **35**, 2413544.
- 6 X. Rui, R. Hua, D. Ren, F. Qiu, Y. Wu, Y. Qiu, Y. Mao, Y. Guo, G. Zhu, X. Liu, Y. Gao, C. Zhao, X. Feng, L. Lu and M. Ouyang, *Adv. Mater.*, 2024, **36**, 2402401.
- 7 S. Chai, Z. Chang, Y. Zhong, Q. He, Y. Wang, Y. Wan, M. Feng, Y. Hu, W. Li, W. Wei and A. Pan, *Adv. Funct. Mater.*, 2023, **33**, 2300425.
- 8 X. Dong, X. Liu, H. Li, S. Passerini and D. Bresser, *Angew. Chem., Int. Ed.*, 2023, **62**, e202308699.
- 9 Y. Sun, M. Pan, Y. Wang, A. Hu, Q. Zhou, D. Zhang, S. Zhang, Y. Zhao, Y. Wang, S. Chen, M. Zhou, Y. Chen, J. Yang, N. Wang and Y. NuLi, *Angew. Chem., Int. Ed.*, 2024, **63**, e202406585.
- 10 D. Fenton, *Polymer*, 1973, **14**, 589.
- 11 Y. Liu, Z. Jin, Z. Liu, H. Xu, F. Sun, X. Q. Zhang, T. Chen and C. Wang, *Angew. Chem.*, 2024, **63**, e202405802.
- 12 Z. Li, L. Sun, L. Zhai, K. S. Oh, J. M. Seo, C. Li, D. Han, J. B. Baek and S. Y. Lee, *Angew. Chem.*, 2023, **135**, e202307459.
- 13 H. Zhang, C. Li, M. Piszcza, E. Coya, T. Rojo, L. M. Rodriguez-Martinez, M. Armand and Z. Zhou, *Chem. Soc. Rev.*, 2017, **46**, 797–815.
- 14 T. Charlesworth, K. Yiamsawat, H. Gao, G. J. Rees, C. K. Williams, P. G. Bruce, M. Pasta and G. L. Gregory, *Angew. Chem., Int. Ed.*, 2024, **63**, e202408246.
- 15 H.-P. Liang, Z. Chen, X. Dong, T. Zinkevich, S. Indris, S. Passerini and D. Bresser, *Macromol. Rapid Commun.*, 2022, **43**, 2100820.
- 16 H.-P. Liang, M. Zarrabeitia, Z. Chen, S. Jovanovic, S. Merz, J. Granwehr, S. Passerini and D. Bresser, *Adv. Energy Mater.*, 2022, **12**, 2200013.
- 17 J. Gao, C. Wang, D.-W. Han and D.-M. Shin, *Chem. Sci.*, 2021, **12**, 13248–13272.
- 18 S. Das, V. G. Pol and V. Adyam, *J. Power Sources*, 2024, **617**, 235160.
- 19 L. Zhao, Y. Du, E. Zhao, C. Li, Z. Sun, Y. Li and H. Li, *Adv. Funct. Mater.*, 2023, **33**, 2214881.
- 20 G. M. Overhoff, E. Verweyen, P. Roering, M. Winter and G. Brunklaus, *ACS Appl. Energy Mater.*, 2024, **7**, 5893–5904.
- 21 C. Li, B. Qin, Y. Zhang, A. Varzi, S. Passerini, J. Wang, J. Dong, D. Zeng, Z. Liu and H. Cheng, *Adv. Energy Mater.*, 2019, **9**, 1970029.
- 22 K. Borzutzki, J. Thienenkamp, M. Diehl, M. Winter and G. Brunklaus, *J. Mater. Chem. A*, 2019, **7**, 188–201.
- 23 A. Mayer, D. Steinle, S. Passerini and D. Bresser, *Nanotechnology*, 2022, **33**, 062002.
- 24 D. Zhou, A. Tkacheva, X. Tang, B. Sun, D. Shanmukaraj, P. Li, F. Zhang, M. Armand and G. Wang, *Angew. Chem., Int. Ed.*, 2019, **58**, 6001–6006.
- 25 H.-D. Nguyen, G.-T. Kim, J. Shi, E. Paillard, P. Judeinstein, S. Lyonnard, D. Bresser and C. Iojoiu, *Energy Environ. Sci.*, 2018, **11**, 3298–3309.
- 26 Z. Chen, D. Steinle, H.-D. Nguyen, J.-K. Kim, A. Mayer, J. Shi, E. Paillard, C. Iojoiu, S. Passerini and D. Bresser, *Nano Energy*, 2020, **77**, 105129.
- 27 Y. Wang, Z. Wu, F. M. Azad, Y. Zhu, L. Wang, C. J. Hawker, A. K. Whittaker, M. Forsyth and C. Zhang, *Nat. Rev. Mater.*, 2024, **9**, 119–133.
- 28 M. L. Meyerson, J. K. Sheavly, A. Dolocan, M. P. Griffin, A. H. Pandit, R. Rodriguez, R. M. Stephens, D. A. V. Bout, A. Heller and C. B. Mullins, *J. Mater. Chem. A*, 2019, **7**, 14882–14894.
- 29 J. Yang, H. Zhang, Q. Zhou, H. Qu, T. Dong, M. Zhang, B. Tang, J. Zhang and G. Cui, *ACS Appl. Mater. Interfaces*, 2019, **11**, 17109–17127.
- 30 Y. Su, X. Rong, H. Li, X. Huang, L. Chen, B. Liu and Y. S. Hu, *Adv. Mater.*, 2023, **35**, 2209402.



31 Y. Zhao, L. Wang, Y. Zhou, Z. Liang, N. Tavajohi, B. Li and T. Li, *Adv. Sci.*, 2021, **8**, 2003675.

32 J. Zhang, J. Zhu, R. Zhao, J. Liu, X. Song, N. Xu, Y. Liu, H. Zhang, X. Wan and Y. Ma, *Energy Environ. Sci.*, 2024, **17**, 7119–7128.

33 C. V. Amanchukwu, A. B. Gunnarsdóttir, S. Choudhury, T. L. Newlove, P. C. Magusin, Z. Bao and C. P. Grey, *Macromolecules*, 2023, **56**, 3650–3659.

34 P. Jagadesan, J. Cui, S. Kalami, L. H. Abrha, H. Lee and H. Khani, *J. Electrochem. Soc.*, 2024, **171**, 040537.

35 X. Zeng, P. Huang, J. Zhou, X. Wei, X. Wang, L. Chen, Y. Ding and J. Fu, *Chem. Eng. J.*, 2024, **487**, 150707.

36 P.-H. Duan, J.-L. Yu, Q.-S. Liu, G. Wu, X.-L. Wang and Y.-Z. Wang, *Adv. Funct. Mater.*, 2024, **34**, 2402065.

37 N. Wang, X. Chen, Q. Sun, Y. Song and T. Xin, *ACS Appl. Mater. Interfaces*, 2023, **15**, 39837–39846.

38 X. Dong, Z. Chen, X. Gao, A. Mayer, H.-P. Liang, S. Passerini and D. Bresser, *J. Energy Chem.*, 2023, **80**, 174–181.

39 C. Han, L. Qiao, G. Xu, G. Chen, K. Chen, S. Zhang, J. Ma, S. Dong, X. Zhou, Y. Han, Z. Cui and G. Cui, *ACS Appl. Mater. Interfaces*, 2024, **16**, 48792–48802.

40 X. Jing, Z. Hu, J. Qin, X. Jiang, M. Wang, S. Huo, S. Zhang, J. Wang and Y. Zhang, *J. Membr. Sci.*, 2023, **688**, 122118.

41 X. Dong, A. Mayer, X. Liu, S. Passerini and D. Bresser, *ACS Energy Lett.*, 2023, **8**, 1114–1121.

42 D. Fraile-Insagurbe, N. Boaretto, I. Aldalur, I. Raposo, F. J. Bonilla, M. Armand and M. Martínez-Ibáñez, *Nano Res.*, 2023, **16**, 8457–8468.

43 W. Fan, Z. Hu, W. Guo, X. Jiang, Y. Yang, Y. Zhang and H. Cheng, *J. Energy Storage*, 2024, **76**, 109594.

44 X. Song, B. Nan, D. Li, Q. Lin, X. Sun, Y. Xue, Q. Cao, X. Gui and K. Xu, *J. Colloid Interface Sci.*, 2023, **647**, 134–141.

45 A. Engler, H. Park, N. Liu and P. A. Kohl, *J. Power Sources*, 2023, **574**, 233145.

46 S. Yun, P. L. Handayani and U. H. Choi, *ChemSusChem*, 2025, e202500684.

47 H. P. K. Ngo, Y. Shao, T. Bertaux, T. K. L. Nguyen, J. Solier, E. Planes, P. Judeinstein, F. Alloin, J.-Y. Sanchez and C. Iojoiu, *ACS Appl. Energy Mater.*, 2025, **8**, 2819–2827.

48 L. Huang, Z. Zhang, S. Huang, S. Wang, D. Han, H. Guo, M. Xiao and Y. Meng, *J. Energy Chem.*, 2025, **104**, 101–110.

49 Z. Song, S. Zhao, X. Shan, J. Tian, N. Muralidharan, J. Zhu, J. Zheng, A. P. Sokolov and P.-F. Cao, *ACS Appl. Mater. Interfaces*, 2025, **17**, 5360–5369.

50 P. L. Handayani, S. Yun, G. Kim and U. H. Choi, *Adv. Energy Mater.*, 2025, **15**, 2405505.

51 Z. Hu, Z. Liu, K. Liu, J. Qin, W. Guo, W. Fan and Y. Zhang, *Sci. China Mater.*, 2025, **68**, 493–502.

52 K. Lu, C. Shan, H. Li, H. Li, H. Zhang, C. Xiong, W. Hu and B. Liu, *Chem. Commun.*, 2025, **61**, 6498–6501.

53 Z. J. Hoffman, A. S. Ho, S. Chakraborty and N. P. Balsara, *J. Electrochem. Soc.*, 2022, **169**, 043502.

54 S. Yun, S. Kim, P. L. Handayani, S. Jung, J. H. Park and U. H. Choi, *Adv. Funct. Mater.*, 2025, 2500232.

55 M. Hahn, D. Rosenbach, A. Kralimowski, T. Nazarenus, R. Moos, M. Thelakkat and M. A. Danzer, *Electrochim. Acta*, 2020, **344**, 136060.

56 R. Soni, J. B. Robinson, P. R. Shearing, D. J. Brett, A. J. Rettie and T. S. Miller, *Energy Storage Mater.*, 2022, **51**, 97–107.

57 J. Tan, J. Matz, P. Dong, J. Shen and M. Ye, *Adv. Energy Mater.*, 2021, **11**, 2100046.

58 H. Zeng, K. Yu, J. Li, M. Yuan, J. Wang, Q. Wang, A. Lai, Y. Jiang, X. Yan, G. Zhang, H. Xu, J. Wang, W. Huang, C. Wang, Y. Deng and S.-S. Chi, *ACS Nano*, 2024, **18**, 1969–1981.

